ARTICLE IN PRESS

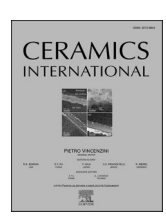
Ceramics International xxx (xxxx) xxx



Contents lists available at ScienceDirect

Ceramics International

journal homepage: www.elsevier.com/locate/ceramint



Reactivity of single, equiatomic and non-equiatomic rare-earth disilicates with CMAS at high temperature

Cynthia Y. Guijosa-Garcia * Peter Mechnich , Uwe Schulz, Ravisankar Naraparaju

Institute for Frontier Materials on Earth and in Space, German Aerospace Center (DLR), 51147, Cologne, Germany

ARTICLE INFO

Handling editor: P. Vincenzini

Keywords: T/EBC Disilicates Multi-component Non-equiatomic CMAS

ABSTRACT

Multi-component $RE_2Si_2O_7$ have gained scientific interest due to their combination of improved properties which can be used for T/EBC (thermal and environmental barrier coating) application. This work addresses the role of Sc^{3+} , Lu^{3+} , Yb^{3+} , Er^{3+} , Y^{3+} , and Ho^{3+} cations in the reactivity with CMAS of single and multi-component rare-earth silicates having either equiatomic or non-equiatomic RE contents. Thermochemical powder interactions were investigated at 1350 and 1400 °C through the reaction products. The reaction products include $RE_2Si_2O_7$, apatite ($Ca_2RE_8(SiO_4)_6O_2$) and pyroxene-type ($Ca(Mg,Fe)[(Si,Al)_2O_6]$) phases. The observed trends indicate that Sc^{3+} , Lu^{3+} , and Yb^{3+} are slowly dissolved in CMAS without causing any crystalline phase formation, meanwhile, Er^{3+} , Y^{3+} , and Ho^{3+} rapidly crystallized the apatite phase. Non-equiatomic multi-component materials can be designed to tune physical, mechanical, environmental, and other relevant properties depending on the concentration of RE elements.

1. Introduction

Higher efficiency in gas-turbine engines requires components to withstand higher temperatures capabilities. Single crystal nickel-based superalloy is the traditionally used material for engine hot section components [1,2]. The current demand to increase the temperature operation limited the component based on nickel-based superalloy. Silicon carbide (SiC) fiber-reinforced SiC ceramic matrix composites (SiC/SiC CMCs) have emerged as a suitable substitution material. CMC offers higher operation temperature resistance and lower densities, significantly reducing the total weight of the engine [3,4]. The extreme combustion environments, such as high velocity and high temperature water vapor, compromises the durability of CMC components. A passivation silica layer is formed in a water vapor environment leading to recession of the surfaces. Therefore, a protection layer called environmental barrier coatings (EBCs) has been introduced to delay the recession. EBCs mainly provide protection against high temperature water vapor [5-7]. An additional environmental issue is the ingestion of siliceous oxides (volcanic ash, sand, and dust) into the engine during service. Siliceous oxides or CMAS (calcium-magnesium-aluminosilicates) melt at ~1200 °C, which is below the turbine inlet temperature, then infiltrate through porosity, consume the coating via chemical reaction, and can induce mechanical failure of the system [8,9]. Thermal barrier coating (TBCs) is an insulated and protective layer based on zirconia material for nickel-based superalloy [2,10]. TBCs, especially ${\rm Gd_2Zr_2O_7}$ or 65YZr (${\rm ZrO_2}$ -65 wt% ${\rm Y_2O_3}$), are recognized for their ability to react with CMAS and yield reaction products such as apatite and garnet that delay the infiltration and consumption of the TBC material and then minimize the CMAS degradation [11–13]. Thermal barrier coatings (TBCs) and environmental barrier coatings (EBCs) are protection systems for components of gas-turbine engines that have enhanced their temperature of operation as a consequence of their thermodynamic efficiency.

Thermal and environmental barrier coatings (T/EBCs) seek to combine the concept of both TBC and EBC and, therefore, their outstanding properties to protect hot section components based on SiC-SiC CMCs [3]. Thus, a T/EBC system must provide thermal and environmental protection for CMCs. Two approaches have described the T/EBC system: 1) a multi-layer system consisting of a silicate-based material (EBC) and a zirconia-based material (TBC) and 2) a single-layer based on a multi-component material [8,14].

Single rare earth disilicates (REDS, RE $_2$ Si $_2$ O $_7$) are front runners as candidates for T/EBCs applications. In particular, REDS with small rare earth (RE) elements, like Sc, Lu, and Yb, are attractive due to their coefficient of thermal expansion (CTE) being close to CMCs (4.5–5.5 x10 $^{-6}$ °C $^{-1}$) and not present polymorphs. Er, Y, and Ho disilicates

E-mail address: cynthia.garcia@dlr.de (C.Y. Guijosa-Garcia).

https://doi.org/10.1016/j.ceramint.2025.08.437

Received 4 July 2025; Received in revised form 15 August 2025; Accepted 30 August 2025 Available online 1 September 2025

 $0272\text{-}8842/ @\ 2025\ The\ Authors.\ Published\ by\ Elsevier\ Ltd.\ This\ is\ an\ open\ access\ article\ under\ the\ CC\ BY\ license\ (http://creativecommons.org/licenses/by/4.0/).$

^{*} Corresponding author.

showed acceptable CTE values, however, undergoing polymorphic transformations (α , β , γ , and δ) leading to CTE changes [15–17]. The phase transformation in REDS (i.e. $\alpha \rightarrow \beta \rightarrow \gamma$) can be avoided by mixing of additional RE³⁺ cations in a solid-solution (multi-component material)

Multi-component disilicates (MC REDS) have attracted significant interest in recent years due to the novelty of the solid-solution design creating strong lattice distortion and resulting in unusual properties, for instance, low thermal conductivity. The thermal conductivity of single disilicates of Sc, Lu, Yb, and Y was reported from $\sim\!2.6\text{--}4.5~\text{W m}^{-1}\text{K}^{-1}$ ($\geq\!1000~^\circ\text{C}$) [14,19,20]. In contrast, a multi-component (Y0.2Yb0.2Sc0.2Gd 0.2Lu 0.2)DS showed a lower thermal conductivity in the range of $\sim\!1.5~\text{W m}^{-1}\text{K}^{-1}$ ($\geq\!1000~^\circ\text{C}$) due to the difference in atomic masses by substitutional-solid-solution phonon-scattering [20]. Multi-component disilicates can offer a significant reduction in thermal conductivity for T/EBC applications.

The original multi-component approach aims to achieve these remarkable properties through the equiatomic ratio of their components [19,20]. Almost all multi-component disilicates reported for T/EBC applications conserve the original concentration, e.g., near-equiatomic ratio. In contrast, non-equiatomic multi-component disilicates have not been reported for T/EBC applications. In the case of high entropy alloys (HEA), non-equiatomic composition with significantly different proportions (Fe $_{40}$ Mn $_{27}$ Ni $_{26}$ Co $_{5}$ Cr $_{2}$) showed single-phase solid-solution successfully and excellent mechanical properties as well [21,22]. Therefore, similar results can be expected when exploring non-equiatomic multi-component disilicates (or monosilicates), which can provide lower thermal conductivity. Hence, non-equiatomic multi-component disilicates are evaluated as potential candidate materials for T/EBCs in this study.

Different methodologies have been used to synthesize disilicate powders, such as co-precipitation, sol-gel, etc., however, the most common and successful homogenization method is the mechanical milling and mixing of oxide powders [23,24]. This method usually requires long milling (~48 h) and heat treatment (~24 h) times [25,26]. An efficient homogenization methodology can reduce this processing time which is very essential in screening many different compositions. In this context, resonance acoustic mixers (RAM) have been used which is time-efficient to reach a homogeneous powder mixture [23].

Single and multi-component REDS have been studied against CMAS corrosion, and it was found out that RE-apatite $(Ca_2RE_8(SiO_4)_6O_2)$ is the main reaction product that can reduce CMAS further attack on EBCs [25–27]. However, its crystallization consumes a larger portion of the material coating, leading to early coating failure. From the extensive studies about CMAS resistance in REDS, the role of each RE³⁺ cation in a multi-component and its reaction products are still under investigation. In TBC materials and CMAS, the changes in solubility for each RE³⁺ cation are more pronounced in the early stages and can be associated to the reactivity [28]. Therefore, this work addresses the evaluation of the effect of Sc^{3+} , Lu^{3+} , Yb^{3+} , Er^{3+} , Y^{3+} , and Ho^{3+} cation on the reactivity of single and equiatomic/non-equiatomic multi-component disilicates with CMAS at high temperatures (1350 and 1400 °C) during the early stage of the reaction up to 1 h.

2. Experimental procedure

2.1. Synthesis of REDS powders

Six single rare earth disilicates of Sc, Lu, Yb, Er, Y, and Ho were synthesized by solid-state reaction of powder mixtures prepared by resonance acoustic mixing, RAM (LabRAM-II, Resodyn, Butte, MT, USA). Sc_2O_3 , Lu_2O_3 (>99.9 %, chempur), Er_2O_3 , Y_2O_3 , Ho_2O_3 (>99.9 %, auer-remy), Yb_2O_3 (>99.5 %, ampere) and SiO_2 nano-powders (>99.5 %, chempur), were used as raw materials in this synthesis process. The powders were mixed in their respective stoichiometric contents with an excess of silica (10 wt%). The amount of extra silica was determined by

several experiments to produce the desirable phase. The powders were mixed with yttria-stabilized $\rm ZrO_2$ balls with 2 mm diameter and deionized water in plastic bottles. The operation conditions of RAM were 100 g acceleration during 10 min or 15 min. The mixed powders were dried on a hot plate under magnetic stirring and later shifted to a box furnace (Ceram-Aix GmbH & Co. KG, D-5100, Germany) where heat treatments were carried out at 1400 °C for yttrium disilicate (YDS), at 1500 °C for holmium disilicate (HoDS), and at 1650 °C for scandium disilicate (ScDS), lutetium disilicate (LuDS), ytterbium disilicate (YbDS), and erbium disilicate (ErDS) for 5 h. The annealing temperatures were initially selected based on the various disilicate phase diagrams, specifically aiming for the β - and γ -polymorph [15] stability regions. The theoretical temperatures were slightly adjusted due to the presence of excess silica in the powder mixtures. The synthesized powders were crushed in a mortar to obtain fine powder.

The respective weight ratios of synthesized single disilicates were used to prepare five equiatomic MCDS and three non-equiatomic MCDS, which are summarized in Table 1. The design of the non-equiatomic MCDS was intended to maximize the influence of both smaller and larger cations such as Sc and Y. The multi-component mixtures were mixed and dried under conditions similar to those of prior single systems. The multi-component systems were isothermally heated at $1650~^{\circ}\mathrm{C}$ for 5 h and crushed using a mortar to reduce the particle size ($\sim\!0.75~-~2~\mu\mathrm{m}$). For the microstructural and chemical analysis, the resulting powders were covered with a carbon-based epoxy (Gatan G1, G2) and were then embedded into an epoxy for standard metallographic preparation.

2.2. REDS powder mixture interactions with CMAS

The interaction experiments were carried out with two different CMAS (CMAS1 and CMAS2). The chemical composition (Table 2), thermal behavior, structural and microstructural properties of these CMAS have been reported elsewhere [29].

Single, equiatomic, and non-equiatomic disilicate powders were mixed with CMAS powders (REDS + CMAS) using mortar in a 60:40 wt ratio. That ratio ensured the continuous formation of reaction products as proposed in early studies [13]. The mixed powders were placed on a platinum foil and heat treated at 1350 and 1400 $^{\circ}\text{C}$ with isothermal hold using a tube furnace (Carbolite Gero GmbH, HTRH 17/70/300, Germany) for 1 h and air quenched to room temperature. The molten mixtures were separated mechanically into two pieces. One-half of the molten samples were ground by mortar to obtain fine powders for x-ray diffraction studies. The second half of the molten samples were placed on an Al_2O_3 plate and covered with an epoxy to follow the same metallographic preparation similar to that of synthetized powders (section 2.1).

2.3. Characterization

Powder x-ray diffraction, XRD, was employed to identify crystalline phases in synthesized REDS (single and multi-component), and the molten powder mixtures (REDS + CMAS). XRD measurements were performed with $CuK\alpha$ ($\lambda = 1.5406 \text{ Å}$) radiation, a step size of 0.01° and a

Table 1Stoichiometry of the synthesized multi-component composition.

System	Multi-component	Abreviation
Equiatomic	$(Y_{0.5}Yb_{0.5})_2Si_2O_7$	MC1
	$(Y_{0.33}Yb_{0.33}Er_{0.33})_2Si_2O_7$	MC2
	$(Y_{0.25}Yb_{0.25}Er_{0.25}Ho_{0.25})_2Si_2O_7$	MC3
	$(Y_{0.2}Yb_{0.2}Er_{0.2}Ho_{0.2}Lu_{0.2})_2Si_2O_7$	MC4
	$(Y_{0.16}Yb_{0.16}Er_{0.16}Ho_{0.16}Lu_{0.16}Sc_{0.16})_2Si_2O_7$	MC5
Non-equiatomic	$(Y_{0.5}Yb_{0.1}Er_{0.1}Ho_{0.1}Lu_{0.1}Sc_{0.1})_2Si_2O_7$	MC6
	$(Sc_{0.4}Lu_{0.2}Yb_{0.2}Er_{0.2})_2Si_2O_7$	MC7
	$(Sc_{0.3}Lu_{0.15}YbO_{0.15}Er_{0.15}Y_{0.25})_2Si_2O_7$	MC8

Table 2 Chemical composition of CMAS [29].

Source	Chemical composition (mol. %)									
	SiO ₂	CaO	MgO	Al_2O_3	FeOx	TiO ₂	SO_3	Ca:Si	Ca:Si with Si extra	
CMAS1	41.7	24.5	12.4	11.0	8.7	1.6	_	0.59	0.43	
CMAS2	35.2	28.5	10.5	9.3	7.3	1.3	7.7	0.80	0.59	

scan rate of 4°/min from 10 to 90 °C in 2-theta (Bruker D8 Advance, Bruker AXS, Karlsruhe, Germany). Identification and quantification of crystal phases were performed by Rietveld method using the EVA/Topas 4.2 software package. The prepared single and multi-component REDS powders, as well as the molten powder mixtures, were microstructurally analyzed by scanning electron microscopy, SEM (DSM Ultra 55, Carl Zeiss NTS, Wetzlar, Germany). The chemical composition of the REDS and molten mixtures was measured using energy dispersive spectroscopy, EDS (UltiMate/Aztec, Oxford Instruments, Abingdon, UK), using backscattering electron mode (BSE). The reaction products and residue melt of the powder mixtures have been analyzed by their corresponding XRD patterns, microstructures and chemical analysis.

3. Results

3.1. Phase formation in single $RE_2Si_2O_7$ and multi-component disilicates $(RE_1^{3+}, RE_2^{3+}, RE_3^{+3} ...)_2Si_2O_7$

Representative XRD diffraction patterns of the synthesized single disilicates systems are presented in Fig. 1. The employed annealing temperatures enabled the formation of the desirable phase. Disilicates of Sc, Lu, Yb, and Y showed monoclinic $\beta\text{-RE}_2\mathrm{Si}_2\mathrm{O}_7$ (C2/m) as the primary phase, while ErDS and HoDS exhibited the $\gamma\text{-RE}_2\mathrm{Si}_2\mathrm{O}_7$ (P21/b) structure (Fig. 1) [15]. An analysis of the structural parameter was also carried out, and a comparison of cell volume and cation radio [51] is shown in Table 3. As expected for single disilicates, the cell volume increases in the order of ScDS < LuDS < YbDS < ErDS < YDS < HoDS, which

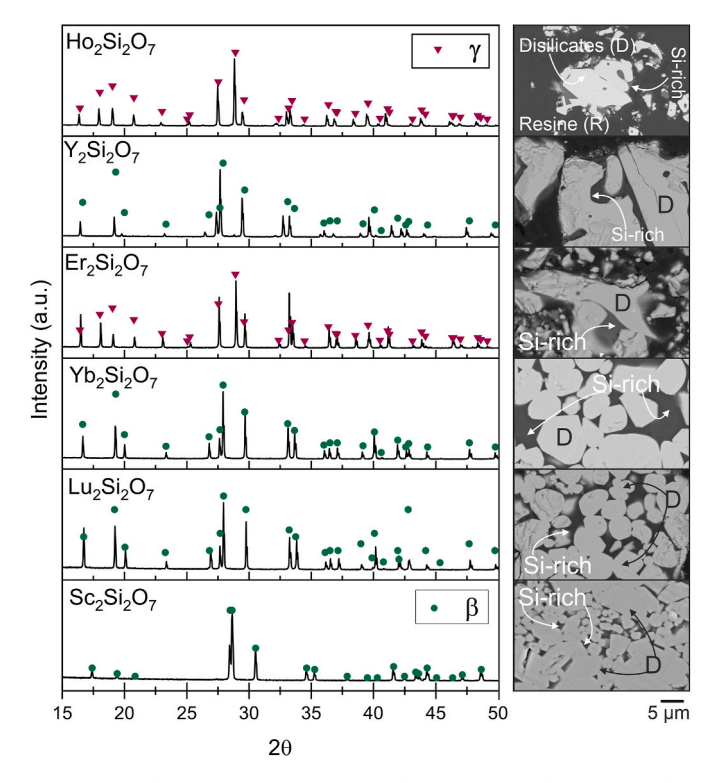


Fig. 1. X-ray diffraction (XRD) patterns and SEM micrographs of the synthesized single $RE_2Si_2O_7$ (RE = Sc, Lu, Yb, Er, Y, and Ho) powders identified as D.

Table 3Summary of cell parameters, volumes and calculated radii of the single disilicates synthesized composition.

System	Abreviation	Volume calculated (ų)	Radius of the cation RE ³⁺ (Å) [51]
Sc ₂ Si ₂ O ₇	ScDS	252.11	0.745
$Lu_2Si_2O_7$	LuDS	275.96	0.861
Yb ₂ Si ₂ O ₇	YbDS	277.96	0.868
Er ₂ Si ₂ O ₇	ErDS	280.29	0.890
$Y_2Si_2O_7$	YDS	285.34	0.900
Ho ₂ Si ₂ O ₇	HoDS	282.96	0.901

corresponds to their RE³⁺ cation size.

Fig. 1 shows the microstructure of the synthesized powders, which exhibit faceted shapes surrounded by a dark Si-rich (confirmed by EDS analysis) phase. The excess SiO_2 that was added during the synthesis might have caused this phase formation. Employing the XRD patterns could not identify any Si crystalline phase. Thus, it is assumed that SiO_2 must be in an amorphous state. In all cases, the XRD structural analysis confirmed that single monoclinic crystalline phases (β or γ) were formed via the applied synthetic method.

Multi-component REDS systems were synthesized using single disilicate powders. In all multi-component systems, the β -phase was found. Also, an additional γ -phase was also observed in $(Y_{0.33}Yb_{0.33}Er_{0.33})_2$. Si $_2O_7$ (MC2) and $(Y_{0.25}Yb_{0.25}Er_{0.25}Ho_{0.25})_2Si_2O_7$ (MC3) as shown in Table 4. The Rietveld method quantification revealed that MC2 presents 83.6 % and 16.4 % of γ and β phase, respectively. On the other hand, MC3 showed 97.3 % of β -phase and 2.7 % of γ -phase. Similarly, to single REDS, XRD did not observe the Si-rich phase.

Generally, the cell volume and radii of equiatomic multi-component REDS can be determined through the average of the single REDS values. However, non-equiatomic multi-component requires a different approach. Therefore, Equation (1) and Equation (2) based on the fractions of volume and radii, are proposed for non-equiatomic MC REDS that can also be used for equiatomic systems.

The calculated lattice parameters and cell volumes for all the MC REDS are shown in Table 4. In general, the cell volume of equiatomic and non-equiatomic multi-component disilicate (V_{mult}) can be determined in terms of the volume of a single REDS (Equation (1)) as the sum of all the volume fractions (χ_{vol}) of each singular system. Rietveld results in Table 4 confirmed that Equation (1).

$$V_{mult} = \sum_{i=1}^{n} \frac{\chi_{vol}(REDS)_i}{\chi_n}$$
 Equation 1

The chemical formula for disilicates can be represented as $A_2Si_2O_7$, where "A" site can incorporate a variety of rare-earth cations e.g., belonging to the $4f^n$ configuration as $La \rightarrow Lu$, also Sc and Y [30]. Hence, multi-component disilicates can be represented as $(RE_1^{3+}, RE_2^{3+}, RE_3^{3+}, RE_2^{3+})$ and $(RE_1^{3+}, RE_2^{3+}, RE_3^{3+})$ cation ("A" site) had shown an effect on the chemical character of the REDS. Similar to the cell volume calculation, the radii of equiatomic and non-equiatomic multi-cations (r_{mult}) can be expressed in terms of cation radii through the sum of radii fraction (χ_{rad}) belonging to each cation into the disilicates (Equation (2)).

$$r_{mult} = \sum_{i=1}^{n} \frac{\chi_{rad} (RE^{3+})_i}{\chi_n}$$
 Equation 2

Table 4Comparison of the lattice parameters, volume and radii for equiatomic and non-equiatomic disilicates.

System	Multi-component	Volume calculated using the Ecuation 1 (\mathring{A}^3)	Volume calculated by Rietveld (Å ³)	Radius calculated using the Ecuation 2.	Phase
Equiatomic	MC1	281.6	281.8	0.884	β
	MC2	281.2	279.0	0.886	β, γ
	MC3	281.6	280.1	0.889	β, γ
	MC4	280.5	281.9	0.884	β
	MC5	275.7	276.1	0.860	β
Non-equiatomic	MC6	279.6	279.9	0.876	β
	MC7	267.6	267.0	0.821	β
	MC8	271.0	272.1	0.846	β

3.2. Reaction behavior of single RE₂Si₂O₇ with CMAS

All the single disilicates exhibited a single reaction product after CMAS interaction, except ScDS (Table 5). The reaction products have not shown significant structural and microstructural differences with respect to the CMAS composition (except ScDS mixtures) or temperature. Fig. 2 presents the reaction product micrographs of single REDS powders with CMAS2 (only for ScDS case reactions with both CMAS1 and CMAS2 are also shown) at 1350 and 1400 °C for 1 h. The reaction products and residue melt of the powder mixtures have been analyzed by their corresponding XRD patterns, microstructures and chemical analysis.

3.2.1. CMAS interactions with single Sc, Lu, and Yb disilicates

The disilicate phase was identified as the only crystalline reaction product for Sc, Lu, and Yb mixtures (Figs. 2 and 3). The disilicate phase corresponds to the monoclinic β -phase (C2/m, space group), which is related to the faceted grains (D) shown in Fig. 2. Moreover, characteristic indication for the amorphous residue melt was observed in the XRD and related to G in Fig. 2. The chemical composition of faceted grains measured by EDS was close to the nominal stoichiometry of RE $_2$ Si $_2$ O $_7$ for RE $_2$ Sc, Lu, and Yb, as shown in Table 6.

The pyroxene-type phase (Py) (Ca(Mg,Fe)[(Si,Al)₂O₆]) was only observed in the ScDS + CMAS2 mixture. This phase is characterized by small crystal formations that surround the REDS grains (Fig. 2). The monoclinic pyroxene phase (C2/c, space group) was identified through the characteristic peaks around 27 and 29° (Fig. 3). The measured chemical composition reveals that such crystals are constituted by Al, Mg, Ca, Fe, and Sc (Table 7). Sc and Si are the main constituents of pyroxene crystals in mixtures at 1350 °C. At 1400 °C, the Sc content decreases while Ca increases. The residual melts (G, in Fig. 2, Appendix 1) contain about 5.5, 4.8, and 8 at. % of Sc, Lu, and Yb, respectively (Fig. 4) at 1350 and 1400 °C. At 1400 °C, the RE concentrations are found to increase. In general, CMAS1 dissolves a lower concentration of RE compared to CMAS2 at 1400 °C.

3.2.2. CMAS interaction with single Er, Y, and Ho disilicates

Apatite phases have been formed in the Er, Y, and Ho mixtures which can easily be identified by their needle-type crystal morphologies (Fig. 2). The respective XRD patterns reveal the characteristic hexagonal crystal structure (P63/m) (Fig. 3). A peak shift of (211) towards higher 20 values typically indicates a decrease in the lattice parameter from Ho

Table 5Summary of reaction products between single REDS with CMAS.

Deposit	Temperature (°C)	ScDS	LuDS	YbDS	ErDS	YDS	HoDS
CMAS1	1350 1400	DS DS	DS DS	DS DS	Ap Ap	Ap Ap	Ap Ap
CMAS2	1350	DS + Pyr	DS	DS	Ap	Ap	Ap
	1400	DS + Pyr	DS	DS	Ap	Ap	Ap

to Er. The chemical composition ($Ca_2RE_8(SiO_4)_6O_2$) of Er-, Y-, and Hoapatite was verified by EDS and presented in Table 8. RE content increases with the RE³⁺ cation size (from Er to Ho) in apatite, as well with the temperature. Only Er-apatite contained Al in the amounts of \sim 5 at. %. Apatites crystallized from Ca-rich deposits, like CMAS2, showed the highest Ca content. Few traces of Mg were also detected (\sim 0.3 at.%) in apatite. The chemical analysis of the residues reveals that Er, Y, and Ho concentrations lie in the range of 7.7–12.1, 6.8–9.3, and 5.8–7.2 at.%, respectively (Fig. 4). Higher concentrations of the RE³⁺ cation were observed for residue mixtures of Er, Y, and Ho compared to Sc, Yb, and Lu mixtures.

3.3. Reaction behavior of multi-component (RE_1^{3+} , RE_2^{3+} , RE_3^{+3} ...) $_2Si_2O_7$ with CMAS

Micrographs of the reaction products formed from MC REDS and CMAS2 interaction after 1 h at 1400 $^{\circ}\text{C}$ are shown in Fig. 5. The effect of each RE³⁺ cation on reaction products was analyzed from a chemical perspective, and the RE content for each reaction product is given in detail below.

3.3.1. CMAS interactions with equiatomic multi-component REDS

Except of MC5, all the equiatomic MC REDS (MC1-MC4) have formed unanimously an apatite phase as a single reaction product. The apatite crystal structure was confirmed through XRD (not shown here), and by the elemental mappings. Apatites are composed of RE^{3+} multications with the chemical formula assumed to be $Ca_2(RE_1^{3+},\ RE_2^{3+},\ RE_3^{3+}\dots)_8(SiO_4)_6O_2$ as showed in Table 9. Fig. 6a depicts the RE^{3+} cation concentration in the apatite structure w.r.t. the RE^{3+} ionic radii in multicomponent REDS. All the MC apatites have slightly higher Er, Y, and Ho concentrations than Yb, Lu, and Sc. MC apatites formed from MC REDS that included Y^{3+} in their initial composition (MC1, MC2, MC3, MC4, and MC5) have shown the highest concentration of Y^{3+} in comparison to other RE^{3+} cations. MC REDS including Sc^{3+} , such as MC5, showed lower concentration values of Sc (1.3 at. %) in the apatite, implying that Sc^{3+} cation is less preferably incorporated into the apatite structure from an equiatomic system.

MC5 was the only equiatomic MC REDS that has formed two reaction products namely the apatite and disilicate. This MC disilicates exhibits higher concentrations of Sc, Lu, and Yb (smaller cations) compared to Er, Y, and Ho (larger cations), see Table 10. A decreasing tendency in the concentration from Sc (10.6 at.%) to Ho (6.4 at.%) is observed in the disilicate phase, and the near-equiatomic ratio was not preserved after the CMAS reactions (Fig. 6b).

The average total concentration of all RE $^{3+}$ cations in the residual melts was measured as \sim 10.5 at. % after 1 h at 1400 °C (CMAS2) as presented in Fig. 7 and Appendix 2. In case of MC1-MC4, where only apatite was formed, the individual contents each RE $^{3+}$ cation values were similar to each other. On the other hand, in case of MC5 Lu and Yb contents were lower to other RE $^{3+}$ cations. Ca concentration in the residue is nearly constant (\sim 18 at. %) for MC1-MC4 where as its content has risen up to 21.2 at. % for MC5. Mg, Al, Fe, and Ti contents are apparently constant in all equiatomic residue glasses (Appendix 2).

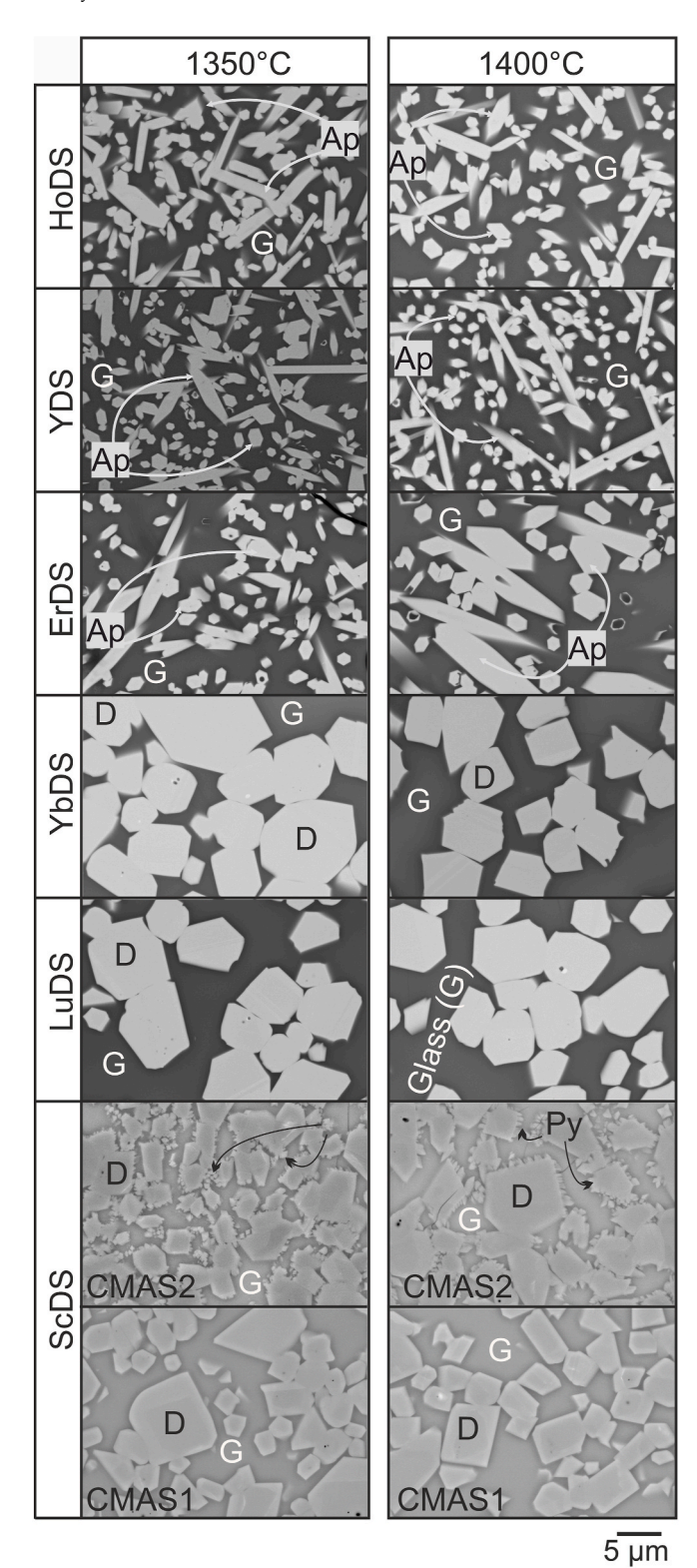


Fig. 2. SEM micrographs of REDS + CMAS powder interactions at 1350 $^{\circ}$ C and 1400 $^{\circ}$ C for 1 h. The reaction products formed between CMAS2 (CMAS1+ScDS) and disilicates of Sc, Lu, Yb, Er, Y, and Ho concerning disilicate (D), apatite (Ap) phases and melt residue (G).

3.3.2. CMAS interaction with non-equiatomic multi-component REDS

The three non-equiatomic MC compositions tested with CMAS yield a single reaction product. The Y-rich non-equatomic MC system (MC6) exhibits an MC apatite crystal (Fig. 5). The apatite shows higher Y-content (27.8 at. %, Table 9), which was intentionally introduced into

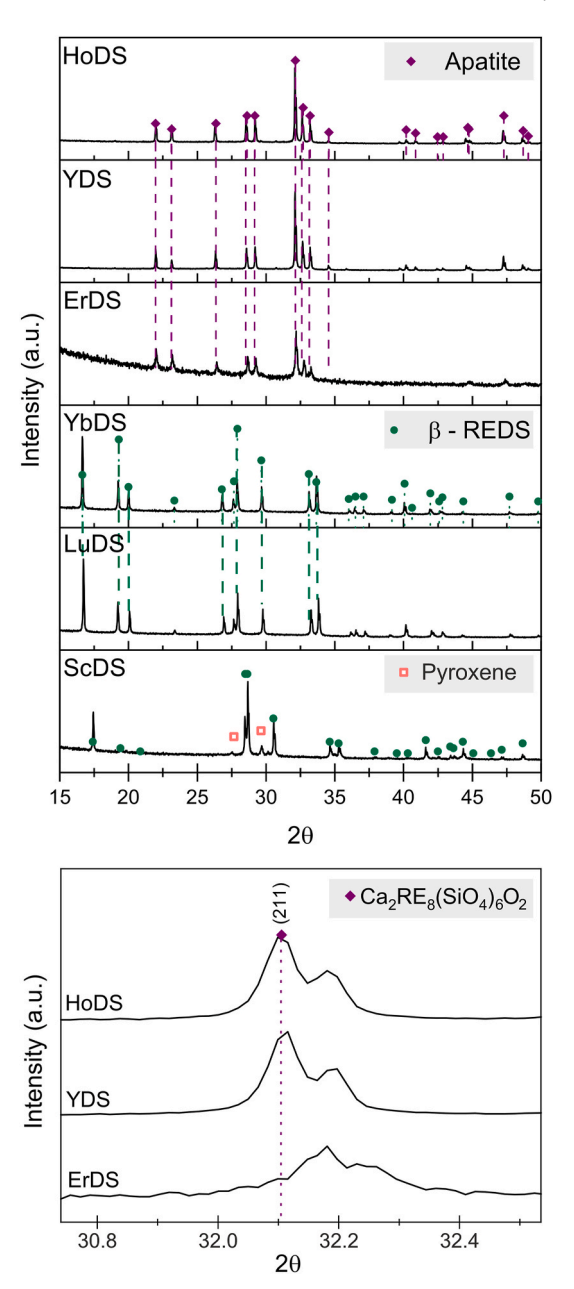


Fig. 3. a) XRD patterns of REDS + CMAS2 powder interactions at 1400 $^{\circ}\text{C}$ for 1 h. b) Comparison of the shift of the (211) peak according to RE $^{3+}$ radii, Er $^{3+}$, Y $^{3+}$, and Ho $^{3+}$.

 Table 6

 Normalized chemical composition of un-reacted REDS.

System	CMAS	Temperature (°C)	Si (at.%)	RE (at.%)
		* ' '	, ,	, ,
ScDS	CMAS1	1350	51.5	48.5
	CMAS1	1400	51.1	48.9
	CMAS2	1350	51.5	48.5
	CMAS2	1400	51.4	48.6
LuDS	CMAS1	1350	52.6	47.4
	CMAS1	1400	52.7	47.3
	CMAS2	1350	52.6	47.4
	CMAS2	1400	52.7	47.3
YbDS	CMAS1	1350	51.4	48.6
	CMAS1	1400	51.5	48.5
	CMAS2	1350	49.5	50.5
	CMAS2	1400	51.4	48.6

Table 7Normalized chemical composition of pyroxene-type phase.

Mixture	Temperature	Si	Al	Mg	Ca	Fe	Sc			
	(°C)	(at.%)	(at.%)							
ScDS + CMAS2	1350	46.0	4.7	8.1	14.6	5.0	21.6			
ScDS + CMAS2	1400	44.9	6.1	10.1	19.4	5.6	13.9			

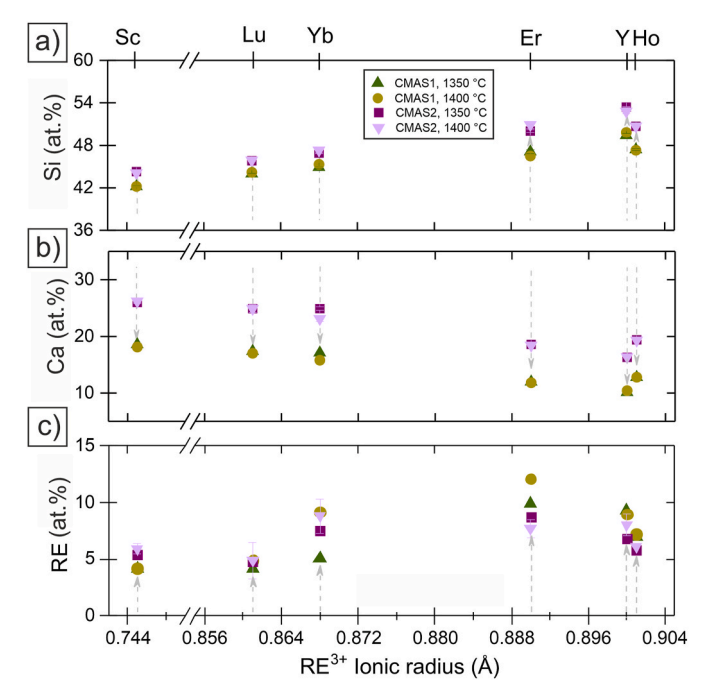


Fig. 4. Si (a), Ca (b), and RE (c) concentration of the residual melt in term of RE $^{3+}$ cation size for single REDS after CMAS interactions (CMAS1 and CMAS2) at 1350 and 1400 °C.

Table 8Normalized chemical composition of crystallized apatites.

		r	· · · · · · · · · · · · · · · · · · ·			
System	CMAS	Temperature (°C)	Si	RE	Ca	Al
			(at.%)			
ErDS	CMAS1	1350	36.5	48.2	10.7	4.6
	CMAS1	1400	36.5	49.1	10.1	4.3
	CMAS2	1350	37.6	45.4	12.3	4.7
	CMAS2	1400	36.1	48.5	11.1	4.3
YDS	CMAS1	1350	40.2	49.4	10.4	-
	CMAS1	1400	38.1	51.5	10.4	-
	CMAS2	1350	40.6	47.2	12.2	-
	CMAS2	1400	38.5	50.1	11.4	-
HoDS	CMAS1	1350	38.8	49.4	11.8	-
	CMAS1	1400	36.2	52.5	11.3	-
	CMAS2	1350	37.3	50.0	12.7	-
	CMAS2	1400	36.1	51.4	12.5	-

the system during the design of a non-equiatomic system (Table 1). For equiatomic MC the resulting apatite does not maintain the initial equal RE^{3+} cation ratio. Instead, the larger presence of larger RE^{3+} cation has been observed which follows the trend i.e., $Sc^{3+} \rightarrow Ho^{3+}$ (Fig. 6).

Sc-rich non-equiatomic MC (MC7) resulted in a non-equiatomic MC disilicate after CMAS interaction. The resulting MC disilicates exhibited larger Sc content (19.3 at. %) as shown in Table 10. In the MC disilicate, ${\rm Lu}^{3+},~{\rm Yb}^{3+},~{\rm and}~{\rm Er}^{3+}$ cations have maintained their initial ${\rm RE}^{3+}$ cation concentration, suggesting no reaction. The combination of higher Sc and Y non-equitomic MC system (MC8) yields the MC disilicate phase as a

reaction product. Compared with the initial composition, the MC disilicate displays slightly higher concentrations of Sc^{3+} and Y^{3+} cations and similar Lu^{3+} , Yb^{3+} , and Er^{3+} values.

The total RE content in the residues are 13.9, 8.4, and 11.3 at. % for MC6, MC7, and MC8, respectively (Fig. 7 and Appendix 2). The enrichment of a specific RE³⁺ cation in the residual melt is consistent with the initial MC REDS design. For example, MC6, with a higher Y ratio (50 %), presents the highest Y content in the glass (6.2 at. %) Fig. 7. The chemical composition of the residual melt reveals a non-equiatomic RE³⁺ cation ratio in the glass. Small cations (Sc^{3+} , Lu^{3+} , and Yb^{3+}) have a larger presence than larger cations (Er^{3+} and Ho^{3+}).

4. Discussion

4.1. Crystallization products of single and MC REDS with CMAS

The CMAS reactivity of six single REDS, five equiatomic MC, and three non-equiatomic MC REDS was evaluated by analyzing their reaction products and residual melts. In the present experiments, the temperature had no significant effect on the formation of reaction products. The slight differences in Ca content between CMAS 1 and 2 led to changes in the reaction product formation only in mixtures containing ScDS. In case of TBCs specifically 65YZr and $Gd_2Zr_2O_7$, the slight differences in the Ca-content between CMAS 1 and 2 have led to a considerable change in reaction product formation especially in terms of apatite or garnet layers [12,13]. The additional silica in the initial REDS powders is assumed to be incorporated into the residual glass components. Consequently, the initial extra SiO_2 content and the Ca:Si ratio were adjusted, resulting in a decreased Ca:Si ratio as depicted in Table 2. No intrinsic crystallization products formed solely from CMAS elements were observed in any of the systems.

The disilicate phase (β, monoclinic) was found as a single reaction product in mixtures of single ScDS, LuDS, and YbDS systems. Similar morphologies of disilicate grains before and after CMAS interaction indicate that the base materials (ScDS, LuDS, and YbDS) have not reacted with CMAS (Figs. 1 and 2). The lower reactivity (microstructural changes) of these DS systems could be also beneficial for blocking the CMAS infiltration given that the coating system is fully dense. However, this inertness could lead into a through-thickness dilatation, which might cause blister cracking, e.g., ScDS [25,31]. Unlike in previous studies, which reported the formation of the Yb-apatite phase in CMAS compositions with higher Ca content (>27 mol%) at elevated temperatures such as 1400 °C, the YbDS system in this work exhibited only the DS phase as the reaction product [26]. The un-reacted Sc, Lu, and Yb disilicates are not considered reactive crystallization products capable of mitigating CMAS infiltration. Thus, the Sc, Lu, and Yb DS systems are rated in this study as being non-protective against CMAS infiltration though their reactivity might change with other CMAS compositions.

Er, Y, and Ho DS have formed a crystalline apatite phase (Ca₂RE₈(-SiO₄)₆O₂) as a reactive crystallization product after CMAS interaction (Figs. 2 and 3). It is generally accepted that apatite is best described by the formula $A_2B_8(TO_4)_6O_2$ where A site prefers Ca^{2+} , Mg^{2+} , and Zr^{4+} cations, B site by RE³⁺ cations while Si⁴⁺ occupies the T site forming the tetrahedral [32,33]. RE-apatites have shown a direct relation between the cation size on the enthalpy formation, unit-cell lattices, etc. For instance, the unit-cell (a, c) increases with larger RE³⁺ cations, i.e. Lu³⁺ (smaller RE) < La³⁺ (larger RE) [34]. In the case of formation enthalpies, there is a lower value for Yb-apatite (smaller RE³⁺) in comparison to Nd-apatite (larger RE³⁺). Moreover, the stability of RE-apatites increases with their RE³⁺ cation size, meaning Y-apatite is more stable than Yb-apatite [35,36]. It is expected that RE-apatites formed from CMAS corrosion with TBC or EBC materials present a similar trend regarding the RE^{3+} cation size. Considering those enthalpy of formation trends, the Er-, Y-, and Ho-apatite are more favorable than Sc-, Lu-, and Yb-apatite [36].

The pyroxene-type phase observed as an additional product only in

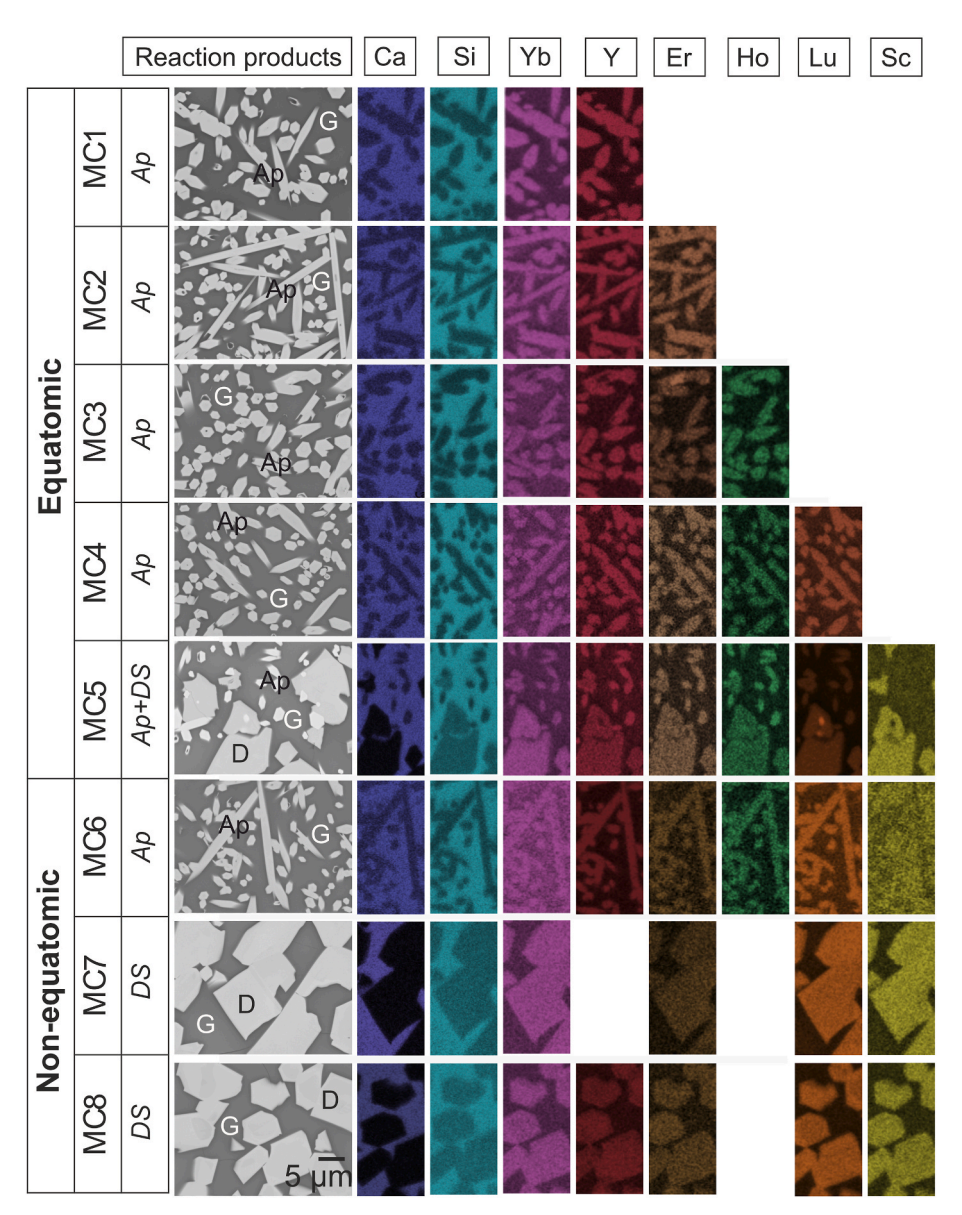


Fig. 5. SEM images and EDS chemical mapping of the reaction products from CMAS2 mixture powder interactions with multi-component disilicates (equiatomic systems = MC1, MC2, MC3, MC4, and MC5, non-equiatomic systems = MC6, MC7, and MC8) at 1400 °C during 1 h.

Table 9 Normalized chemical composition of crystallized MC apatites at 1350 $^{\circ}$ C and CMAS2

System	Si	Ca	Sc	Lu	Yb	Er	Y	Но
	(at.%)							
MC1	38.2	13.0	_	-	22.8	-	26.0	_
MC2	38.1	12.6	_	_	16.1	16.2	17.0	_
MC3	37.7	12.2	_	_	11.7	12.7	13.2	12.5
MC4	37.5	12.0	_	8.7	9.6	10.5	11.1	10.6
MC5	37.2	12.9	1.7	7.8	9.1	10.7	10.6	10.8
MC6	38.1	12.9	1.3	4.2	5.0	5.3	27.8	5.4

the case of ScDS when reacted with CMAS2 (Fig. 2), which is promoted by the presence of other elements such as Si, Mg, Sc, and Ca. Based on the nominal chemical composition (Ca(Mg,Fe)[(Si,Al)₂O₆), pyroxenetype can be denoted as (Mg_{0.34}Fe_{0.19}Sc_{0.47})Ca(Si_{0.9}Al_{0.1})₂O₆ (1400 °C) considering the substitution model [33]. The pyroxene crystals grow when the temperature increases, as shown in Fig. 2.

The partition coefficient (D) is described as the ratio of a specific

element distributed between two different phases in equilibrium [37, 38]. The concept of partition coefficient has been used to evaluate the preferential formation of apatite and garnet of various RE³⁺ cations when reacted to CMAS [37,38]. Fig. 8 presents the apatite and garnet partition coefficient as a function of the RE³⁺ cation radius reported by Poerschke et al. [37]. In addition, the partition coefficients of pyroxene (clinopyroxene, green zone) and a complementary zone for apatite and garnet related to the Sc³⁺ cation (dotted zone) were included. The additional zones were plotted based on the partition coefficient collected from geological data [39–45]. On the other hand, the partition coefficient of Er-, Y-, Ho-apatite, and Sc-pyroxene, are calculated from this study, is presented in Fig. 8 (grey and purple symbols). According to the Dapatite, all the apatites (Er, Y, and Ho) were found in the predicted apatite zone proposed in the literature [37].

Fig. 8 shows a relation between the partition coefficients of pyroxene and the RE^{3+} cations. With the exception of Sc^{3+} , all the RE^{3+} cations presented a partition coefficient below 1, suggesting a low tendency to form pyroxenes. In the case of Sc^{3+} , the partition coefficients (literature and calculated) are mostly above 1, indicating a tendency to form pyroxene. For the Sc^{3+} cation, the D for apatite and pyroxene shows a

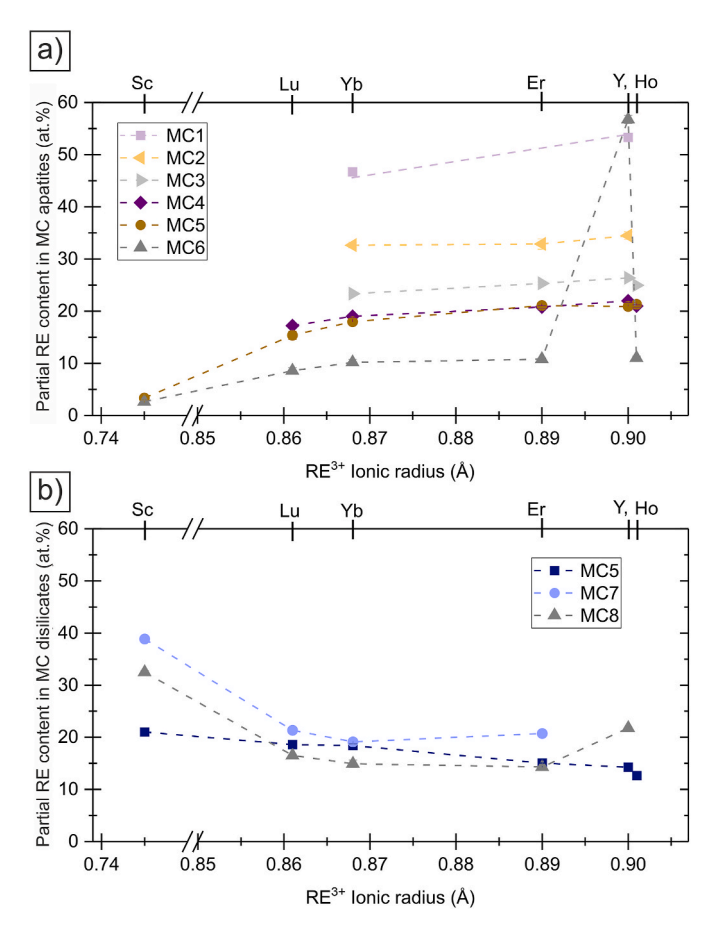


Fig. 6. Comparison contents of Sc³⁺, Lu³⁺, Yb³⁺, Er³⁺, Y³⁺, and Ho³⁺ in multicomponent apatite (a), disilicates (b) phases after CMAS2 interaction at 1400 $^{\circ}$ C for 1 h. Note that MC5 is the only system which forms both Ap + REDS.

Table 10 Normalized, chemical composition of crystallized MC disilicate at 1350 $^{\circ}\text{C}$ and CMAS2.

System	Si	Sc	Lu	Yb	Er	Y	Но
	(at.%)						
MC5	49.5	10.6	9.4	9.3	7.6	7.2	6.4
MC7	50.3	19.3	10.6	9.5	10.3	-	-
MC8	50.4	16.1	8.2	7.4	7.1	10.8	-

contrary tendency, e.g., higher D for pyroxene than apatite. This result agrees with the absence of an apatite phase in Sc mixtures in the current study. From the diagram, the trend to form garnet increases with small cations including Sc³⁺. However, garnets were not observed in any of the RE³⁺ cations studied. Nevertheless, the observed pyroxene phase might have been formed due to the higher Ca content in CMAS2, which can lead to secondary reaction products after extended periods of time. Another hypothesis is that the pyroxene could have been crystallized during cooling. The present study cannot prove the protection of the pyroxene phase against CMAS.

4.2. Residual melts in single REDS mixtures

Even though no reaction products were observed in Sc, Lu, and Yb mixtures, their residual melts showed certain amount of RE as evidence of the dissolution of the initial material after 1 h at 1350 and 1400 °C (Fig. 4c). The amount of SiO₂ in the residual melt increases with larger RE³⁺ cations like Er³⁺, Y³⁺, and Ho³⁺. Meanwhile, Sc³⁺, Lu³⁺, and Yb³⁺ cations showed lower concentrations suggesting a slow dissolution or

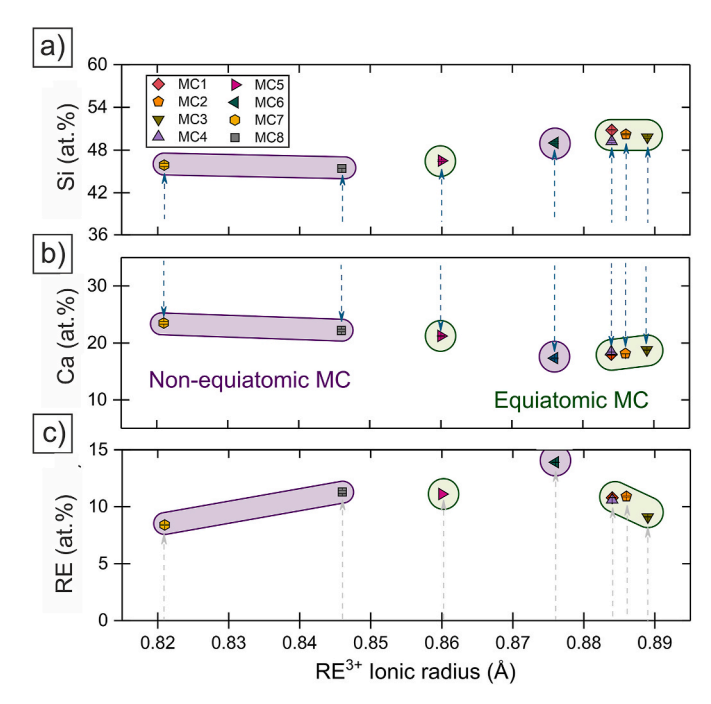


Fig. 7. Si (a), RE (b), and Ca (c) concentration of the residual melt in term of RE $^{3+}$ cation size for MC REDS after CMAS interactions (CMAS2) at 1400 °C.

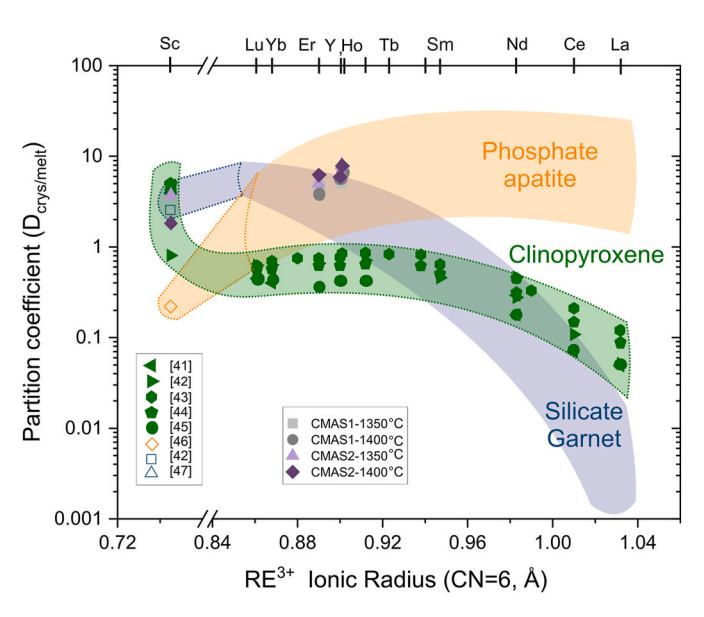


Fig. 8. Comparison of partition coefficient between clinopiroxenes, phosphate apatite and garnet.

lower reactivity with CMAS, which could not form reaction products like apatite (Fig. 4a). Nonetheless, a time-based study should be conducted to determine the reaction kinetics, which was beyond the scope of this research. Slightly higher Si values were observed in case of Y compared to Ho interactions. This behavior may be associated with the different electronic configurations of Y^{3+} or the thermal stability of Y-apatite [30, 46].

Additionally, the Ca content in the residue decreases for all the mixtures, even in residues where no apatite is crystallized (Fig. 4b). Especially, lower values of Ca in Sc, Lu, and Yb do not correspond to any apatite formation. The Ca ions are substituted by RE³⁺ cation in the melt. However, the absence of Ca in the reaction product cannot be explained. From chemical analysis, Mg, Fe, and Ti concentrations are

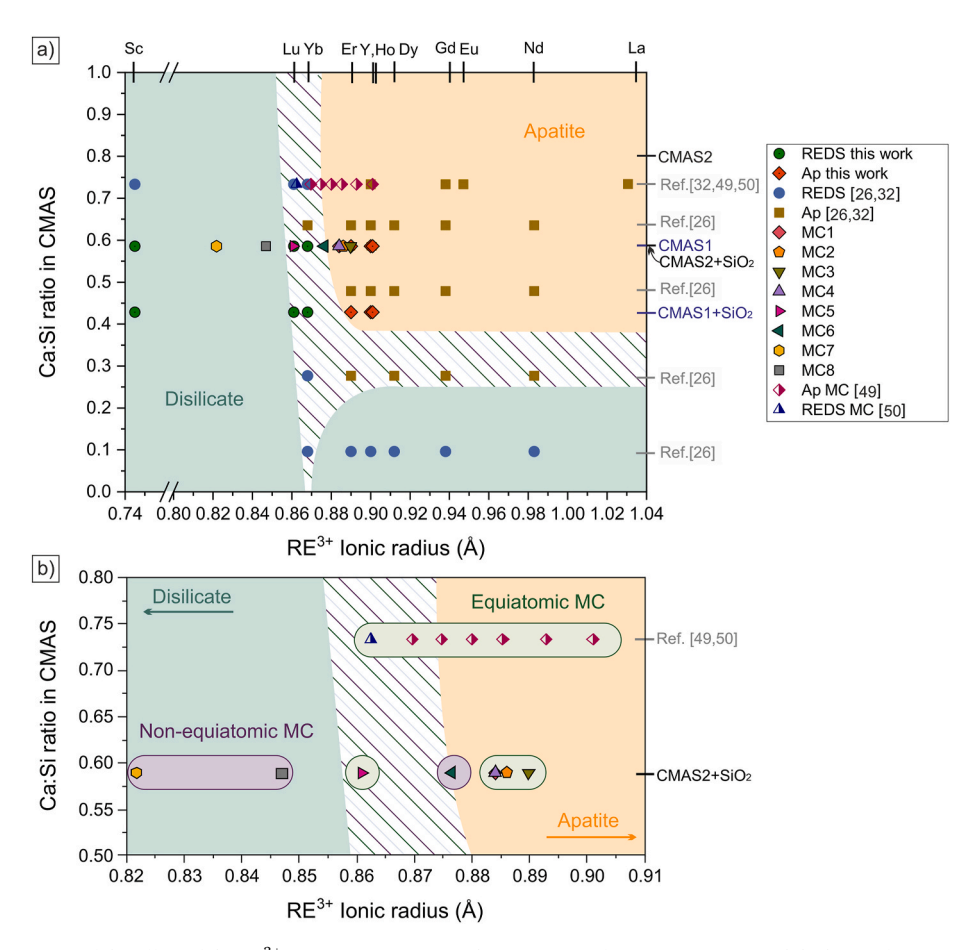


Fig. 9. Schematic representation of the effect of the RE^{3+} cations $(RE_2Si_2O_7)$ and Ca:Si ration of CMAS on apatite and disilicates formation as a reaction product (a). MC REDS are plotted in terms of the calculated radio using Equation (1).

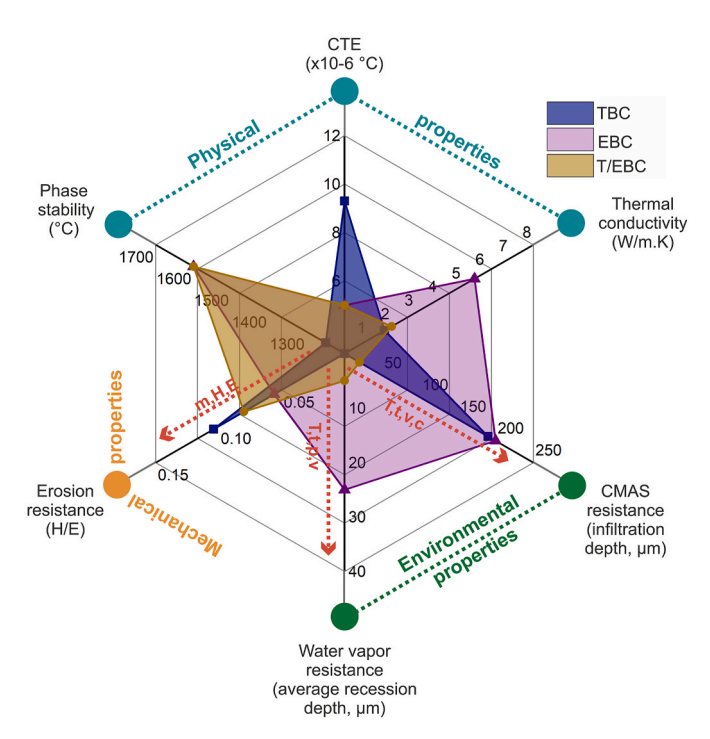


Fig. 10. Comparison of state-of-the-art TBC, EBC, and proposed T/EBC concepts in terms of physical, mechanical and environmental properties. $^*T = Temperature$, t = time, p = pressure and v = velocity.

apparently constant for both CMAS compositions and temperatures and do not contribute to the formation of primary or secondary reaction products, with the exception of ScDS. For larger atomic radii, the lower presence of Ca and higher presence of Si in the melt explain the formation of apatites. Slight variations in Ca and Si content for Y and Ho might indicate that Y has a higher reactivity compared to Ho.

4.3. Effect of multi-cations on reaction products

Upon reaction with CMAS equiatomic and non-equiatomic MC systems have resulted in either un-reacted MC disilicates and/or crystallized into MC RE-apatite (Fig. 7). In the case of MC apatite (Fig. 6a), the results indicate a clear tendency of higher presence for larger RE $^{3+}$ cation constituents (Er $^{3+}$, Y $^{3+}$, and Ho $^{3+}$). In general, A and B sites in A₂B₈(TO₄)₆O₂, are preferentially occupied by Ca $^{2+}$ and RE $^{3+}$ cations [32,33]. The B site can also be occupied by Ho $^{3+}$, Y $^{3+}$, Er $^{3+}$, ... etc., in a solid solution to form a multi-component apatite. Additionally, the A and B sites should be similar in size. Due to a larger difference between the radii of Ca (1.12 Å) and Sc (0.745 Å), Lu (0.861 Å), and Yb (0.868 Å), apatite formation tendency decreases for single and multi-component systems consisting of those respective RE $^{3+}$.

On the other hand, the enthalpy of formation (ΔH°) plays an important role in the crystallization of apatites. The enthalpy of formation of apatites based on a single RE³⁺ cation such as Yb- Er-, Y-, and Ho-apatite have been reported as -407.56 ± 16.64 , -542.31 ± 13.90 , -622.45 ± 11.05 , and -643.60 ± 4.17 (kJ mol⁻¹), respectively where Ca₂Ho₈(SiO₄)₆O₂ is more stable that Ca₂Yb₈(SiO₄)₆O₂ [36,47]. Therefore, under equilibrium conditions Ho-apatite formation is considered more favorable than Yb-apatite. In general, the RE³⁺ cation size has a direct correlation to the enthalpy of formation of RE-apatites

 $(Ca_2RE_8Si_6O_{26} \ and \ RE_{9.33} \square_{0.67}Si_6O_{26})$, where larger RE^{3+} ionic radii exhibit lower values of ΔH° e.g. $Ca_2Nb_8(SiO_4)_6O_2$, -845.72 \pm 27.54 than smaller RE^{3+} ionic e.g., $Ca_2Yb_8(SiO_4)_6O_2$, -407.56 \pm 16.64 (kJ mol⁻¹) [36]. In multi-component apatites, it is anticipated that the contribution of the formation enthalpy will be accordingly to the fraction of the RE^{3+} cation. Thus, multi-component apatites involving more significant amounts of larger RE^{3+} cations are expected to have lower values of ΔH° . The contribution of these enthalpies can be related to the higher content of Ho, Y, and Er in the apatite structure for equiatomic multi-component presented in Fig. 6a.

Additionally, MC disilicates as products show a reverse tendency w.r. t. the RE³⁺ ionic sizes (Fig. 6b). i.e., higher radii RE³⁺ elements show less presence in MC REDS. This tendency is in good agreement with single REDS systems where Sc, Lu, and Yb exhibit more disilicates.

In general, equiatomic and non-equiatomic multi-component disilicates have formed non-equiatomic disilicates as reaction/precipitation products.

4.4. Residual melts in multi-component mixtures

In equiatomic MC REDS mixtures, irrespective of the reaction products, similar RE concentrations were found in the glassy residues (Fig. 7). In non-equiatomic MC residues, the tendency has a direct dependency on the initial RE concentration before the reaction. The Ca consumption is led by the apatite formation regardless of equiatomic or non-equiatomic MC. However, the Ca consumption is higher in residues from MC with higher ionic radii, i.e. MC1, MC2. As expected, Si contents increase with the dissolution of MC REDS. The Si concentration is slightly lower for the MC REDS system, where apatite is formed, than in Er, Y, or Ho systems with the same reaction product. Comparing single and MC REDS in terms of the chemical composition, it can be concluded that the dissolution and reactivity will depend on the RE³⁺ cation(s) size that constituted the initial single or MC REDS system (Equation (1) and Equation (2)).

4.5. Trend of CMAS reaction products based on atomic radii

In terms of CMAS reaction with single and multi-component REDS, in addition to the $\mbox{\rm RE}^{3+}$ ionic radii the Ca: Si ratio in CMAS was identified as one key criterion for forming reaction products such as apatite or garnet. Fig. 9 depicts the dependency of Ca:Si ratio and the RE³⁺ ionic radii on the reaction product formation using the current and results literature data (single and multi-component) [26,31,48,49]. It is worth mentioning that the Ca:Si ratio for the present mixtures has been calculated assuming the extra silica was incorporated into the residue glass (Table 2). Based on the comparison, two main zones were identified: a) disilicate (blue) and b) apatite (orange) (Fig. 9a). The disilicate zone was associated with two ranges, the first was the combination of the entire Ca:Si range with RE^{3+} radii between $\sim 0.74-0.86$ Å. The second corresponds to Ca:Si ratio from ~ 0 to 0.22 and RE³⁺ radii between \sim 0.87–1.04 Å. The apatite zone is related to a Ca:Si ratio of about 0.4–1 and RE^{3+} radii between $\sim\!0.88\text{--}1.04$ Å. Few compositions were found in between apatite and disilicate zones (i.e., YbDS). Thus, a third zone (zebra) was plotted as an intermediate zone where both reaction products might form. Additional data points are required to visualize the total range for Ca:Si ratio and RE³⁺ cations.

Fig. 9b displays the relation of calculated multi-component RE³⁺ ionic radii (Equation (1)) with Ca/Si ratio and apatite/DS formation. MC5 (equiatomic), MC7, and MC8 (non-equiatomic) are in the region of disilicate formers. Meanwhile, MC1, MC2, MC3, MC4, MC5, and MC6 are classified as apatite formers. MC5 (equiatomic) could be found in a dual zone, suggesting both apatite and disilicate formation under given conditions (Fig. 5). This trend is quite similar to the observation in single REDS shown in Fig. 9a, which confirmed the preference for larger RE³⁺ cations (single or MC) to form apatite with Ca-rich CMAS. Thus, smaller RE³⁺ cations (single or MC) and Ca-low CMAS are strongly correlated to

disilicate reaction products.

4.6. Towards the design of T/EBC systems

Assuming that the apatite phase provides enough protection against CMAS, all equi- and non-equiatomic MC REDS except MC7 and MC8 compositions are attractive candidates for T/EBC (single- or multi-layer). However, their thermal conductivity, toughness, and water vapor stability properties should match the range indicated in the spider diagram Fig. 10 [50].

Selecting the appropriate composition from the huge number of probable multi-component systems demands for a robust and efficient strategy. The combination of experimental and theoretical data can lead to an optimized scanning of relevant behavior under different critical properties. Ongoing efforts focus on integrating this methodology into the screening of thermal and environmental properties for multi-component T/EBC candidates.

5. Conclusions

A novel synthesis method was developed for rapid production of single REDS, equi- and non-equiatomic MC REDS powders for application as thermal and environmental barrier coatings. Irrespective of the number of RE $^{3+}$ cations present, all the synthesized compositions exhibited high temperature stable, single phase β - and $\gamma\text{-RE}_2\text{Si}_2\text{O}_7$. The CMAS reactivity of all the produced REDS powders was tested at high temperature for two CMAS compositions, and the reaction products were studied in detail. There was a clearly tendency in terms of reaction products and the RE $^{3+}$ cation size for all single and MC REDS. The important findings after the reaction with CMAS are summarized below:

- The disilicate reaction product is dominant in CMAS interaction with single or multi-component REDS constituted by Sc³⁺, Lu³⁺, and Yb³⁺ (small radii). This trend is similar in both equi- and non-equiatomic multi-component REDS.
- Apatite is a predominant reaction product formed for single or equiatomic REDS based on Er³⁺, Y³⁺, and Ho³⁺ (larger radii). In case of non-equiatomic multi-component REDS based on larger cations, apatites have also been formed.
- The pyroxene phase as a secondary reactive product grows preferentially in mixtures with small RE cations e.g. Sc, which limits the possibility to form with other RE³⁺ cations
- The chemical composition of the residual melts reveals that larger RE cations consume more Ca to crystallize apatite whereas smaller RE cations dissolve slowly and reprecipitate in to disilicates.
- In case of non equiatomic multi-component REDS systems, it is
 promising to increase the share of larger RE cations such as Y³⁺, e.g.,
 (Y_{0.5}Yb_{0.1}Er_{0.1}Ho_{0.1}Lu_{0.1}Sc_{0.1})₂Si₂O₇, which increases the effectiveness to promote CMAS resistance and the remaining RE compositions can be used for tuning other properties.

CRediT authorship contribution statement

Cynthia Y. Guijosa-Garcia: Writing – original draft, Visualization, Methodology, Investigation, Formal analysis, Data curation, Conceptualization. Peter Mechnich: Writing – review & editing, Validation, Methodology. Uwe Schulz: Writing – review & editing, Validation. Ravisankar Naraparaju: Writing – review & editing, Validation, Supervision.

Declaration of competing interest

The authors declare the following financial interests/personal relationships which may be considered as potential competing interests: Cynthia Y. Guijosa-Garcia reports financial support was provided by German Academic Exchange Service, German Academic Exchange

Service (DAAD), Germany. If there are other authors, they declare that they have no known competing financial interests or personal relationships that could have appeared to influence the work reported in this paper.

Acknowledgments

The authors acknowledge the support of the German Academic Exchange Service (DAAD). Jan E. Förster for providing technical support for interaction experiments.

Appendix A. Supplementary data

Supplementary data to this article can be found online at https://doi.org/10.1016/j.ceramint.2025.08.437.

References

- D.R. Clarke, M. Oechsner, N.P. Padture, Thermal-barrier coatings for more efficient gas-turbine engines. MRS Bull. 37 (2012) 891–898.
- [2] A.G. Evans, D.R. Clarke, C.G. Levi, The influence of oxides on the performance of advanced gas turbines, J. Eur. Ceram. Soc. 28 (2008) 1405–1419, https://doi.org/ 10.1016/j.jeurceramsoc.2007.12.023.
- [3] N.P. Padture, Advanced structural ceramics in aerospace propulsion, Nat. Mater. 15 (2016) 804–809. https://doi.org/10.1038/nmat4687
- 15 (2016) 804–809, https://doi.org/10.1038/nmat4687.
 [4] E. Bakan, D.E. Mack, G. Mauer, R. Vaßen, J. Lamon, N.P. Padture, Advanced Ceramics for Energy Conversion and Storage, 2020, pp. 3–62.
- K.N. Lee, Environmental barrier coatings for SiC_f/SiC, in: Ceramic Matrix Composites: Materials, Modeling and Technology, 2014, pp. 430–451, https://doi. org/10.1002/9781118832998.ch15.
- [6] K.N. Lee, Protective coatings for gas turbines, The gas turbine handbook 4 (2)
- [7] N.P. Padture, Npj mater degrad, environmental degradation of high-temperature protective coatings for ceramic-matrix composites in gas-turbine engines 3. htt ps://doi.org/10.1038/s41529-019-0075-4, 2019.
- [8] D.L. Poerschke, D.D. Hass, S. Eustis, G.G.E. Seward, J.S. Van Sluytman, C.G. Levi, S. Sampath, Stability and CMAS resistance of Ytterbium-Silicate/Hafnate EBCs/TBC for SiC composites, J. Am. Ceram. Soc. 98 (2015) 278–286, https://doi.org/10.1111/jace.13262
- [9] B.J. Harder, J.L. Stokes, B.A. Kowalski, J. Stuckner, J.A. Setlock, Steam oxidation performance of Yb2Si2O7 environmental barrier coatings exposed to CMAS, J. Eur. Ceram. Soc. 44 (2024) 2486–2498, https://doi.org/10.1016/j. jeurceramsoc.2023.10.073.
- [10] R. Naraparaju, M. Hüttermann, U. Schulz, P. Mechnich, Tailoring the EB-PVD columnar microstructure to mitigate the infiltration of CMAS in 7YSZ thermal barrier coatings, J. Eur. Ceram. Soc. 37 (2017) 261–270, https://doi.org/10.1016/j.jeurceramsoc.2016.07.027.
- [11] S. Krämer, J. Yang, C.G. Levi, Infiltration-inhibiting reaction of gadolinium zirconate thermal barrier coatings with CMAS melts, J. Am. Ceram. Soc. 91 (2008) 576–583, https://doi.org/10.1111/j.1551-2916.2007.02175.x.
- [12] C. Mikulla, L. Steinberg, P. Niemeyer, U. Schulz, R. Naraparaju, Microstructure refinement of EB-PVD gadolinium zirconate thermal barrier coatings to improve their CMAS resistance, Coatings 13 (2023), https://doi.org/10.3390/ coatings13050905.
- [13] R. Naraparaju, J.J.G. Chavez, U. Schulz, C.V. Ramana, Interaction and infiltration behavior of Eyjafjallajökull, Sakurajima volcanic ashes and a synthetic CMAS containing FeO with/in EB-PVD ZrO 2 -65 wt% Y 2 O 3 coating at high temperature, Acta Mater. 136 (2017) 164–180, https://doi.org/10.1016/j. actamat 2017 06 055
- [14] L.R. Turcer, N.P. Padture, Towards multifunctional thermal environmental barrier coatings (TEBCs) based on rare-earth pyrosilicate solid-solution ceramics, Scr. Mater. 154 (2018) 111–117, https://doi.org/10.1016/j.scriptamat.2018.05.032.
- [15] J. Felsche, Polymorphism and crystal data of the rare-earth disilicate of type RE2Si2O7, J. Less Common. Met. 2I (1970).
- [16] A.J. Fernández-Carrión, M. Allix, A.I. Becerro, M. White, Thermal expansion of rare-earth pyrosilicates, J. Am. Ceram. Soc. 96 (2013) 2298–2305, https://doi.org/ 10.1111/jcpc.13288
- [17] A. Escudero, M.D. Alba, A.I. Becerro, Polymorphism in the Sc2Si2O7-Y2Si2O7 system, J. Solid State Chem. 180 (2007) 1436–1445, https://doi.org/10.1016/j. issc.2006.11.029.
- [18] H. Ohashi, M.D. Alba, A.I. Becerro, P. Chain, A. Escudero, Structural study of the Lu2Si2O7–Sc2Si2O7 system, J. Phys. Chem. Solid. 68 (2007) 464–469, https://doi. org/10.1016/j.jpcs.2006.12.025.
- [19] X. Wang, Y. He, C. Wang, Y. Bai, F. Zhang, Y. Wu, G. Song, Z.J. Wang, Thermal performance regulation of high-entropy rare-earth disilicate for thermal environmental barrier coating materials, J. Am. Ceram. Soc. 105 (2022) 4588–4594, https://doi.org/10.1111/jace.18456.
- [20] L.R. Turcer, A. Sengupta, N.P. Padture, Low thermal conductivity in high-entropy rare-earth pyrosilicate solid-solutions for thermal environmental barrier coatings, Scr. Mater. 191 (2021) 40–45, https://doi.org/10.1016/j.scriptamat.2020.09.008.

- [21] K.G. Pradeep, C.C. Tasan, M.J. Yao, Y. Deng, H. Springer, D. Raabe, Non-equiatomic high entropy alloys: approach towards rapid alloy screening and property-oriented design, Mater. Sci. Eng., A 648 (2015) 183–192, https://doi.org/10.1016/j.msea.2015.09.010.
- [22] M.J. Yao, K.G. Pradeep, C.C. Tasan, D. Raabe, A novel, single phase, non-equiatomic FeMnNiCoCr high-entropy alloy with exceptional phase stability and tensile ductility, Scr. Mater. 72–73 (2014) 5–8, https://doi.org/10.1016/j.scriptamat.2013.09.030.
- [23] G. Álkan, P. Mechnich, J. Pernpeintner, Improved performance of ceramic solar absorber particles coated with black oxide pigment deposited by resonant acoustic mixing and reaction sintering, Coatings 12 (2022), https://doi.org/10.3390/ coatings12060757.
- [24] P. Mechnich, G. Alkan, Rapid evaluation of the particle-erosion resistance of Al2O3 ceramics, composites, and coatings using a resonant acoustic mixer, Adv. Appl. Ceram. 122 (2023) 250–257, https://doi.org/10.1080/17436753.2023.2231230.
- [25] L.R. Turcer, A.R. Krause, H.F. Garces, L. Zhang, N.P. Padture, Environmental-barrier coating ceramics for resistance against attack by molten calcia-magnesia-aluminosilicate (CMAS) glass: part II, β-Yb2Si2O7 and β-Sc2Si2O7, J. Eur. Ceram. Soc. 38 (2018) 3914–3924, https://doi.org/10.1016/j.jeurceramsoc.2018.03.010.
- [26] J.L. Stokes, B.J. Harder, V.L. Wiesner, D.E. Wolfe, Effects of crystal structure and cation size on molten silicate reactivity with environmental barrier coating materials, J. Am. Ceram. Soc. 103 (2019) 622–634, https://doi.org/10.1111/ iace_16694.
- [27] L.R. Turcer, A.R. Krause, H.F. Garces, L. Zhang, N.P. Padture, Environmental-barrier coating ceramics for resistance against attack by molten calcia-magnesia-aluminosilicate (CMAS) glass: part I, YAIO3 and γ-Y2Si2O7, J. Eur. Ceram. Soc. 38 (2018) 3905–3913, https://doi.org/10.1016/j.jeurceramsoc.2018.03.021.
- [28] D.L. Poerschke, T.L. Barth, C.G. Levi, Equilibrium relationships between thermal barrier oxides and silicate melts, Acta Mater. 120 (2016) 302–314, https://doi.org/ 10.1016/j.actamat.2016.08.077.
- [29] R. Naraparaju, P. Mechnich, U. Schulz, G.C. Mondragon Rodriguez, S. Sampath, The accelerating effect of CaSO4 within CMAS (CaO-MgO-Al2O3-SiO2) and its effect on the infiltration behavior in EB-PVD 7YSZ, J. Am. Ceram. Soc. 99 (2016) 1398-1403, https://doi.org/10.1111/jace.14077.
- [30] R.D. Shannon, Revised effective ionic radii and systematic studies of interatomic distances in halides and chalcogenides, Acta Crystallogr. A 32 (1976) 751–767, https://doi.org/10.1107/s0567739476001551.
- [31] J. Felscher, The crystal chemistry of the rare-Earth Silicates, Struct. Bond 13 (1973), https://doi.org/10.1007/3-540-06125-8 3.
- [32] J. Liu, L. Zhang, Q. Liu, L. Cheng, Y. Wang, Calcium-magnesium-aluminosilicate corrosion behaviors of rare-earth disilicates at 1400°C, J. Eur. Ceram. Soc. 33 (2013) 3419–3428, https://doi.org/10.1016/j.jeurceramsoc.2013.05.030.
- [33] E. Godbole, A.v.d. Handt, D. Poerschke, Apatite and garnet stability in the Al-Ca-Mg-Si-(Gd/Y/Yb)-O systems and implications for T/EBC: CMAS reactions, J. Am. Ceram. Soc. 105 (2021) 1596–1609, https://doi.org/10.1111/jace.18179.
- [34] P. Mechnich, W. Braue, D.J. Green, Volcanic ash-induced decomposition of EB-PVD Gd2Zr2O7 thermal barrier coatings to Gd-Oxyapatite, zircon, and Gd,Fe-Zirconolite, J. Am. Ceram. Soc. 96 (2013) 1958–1965, https://doi.org/10.1111/ jace.12251.
- [35] J.V. Crum, S. Chong, J.A. Peterson, B.J. Riley, Syntheses, crystal structures, and comparisons of rare-earth oxyapatites Ca2RE8(SiO4)6O2 (RE = La, Nd, Sm, Eu, or Yb) and NaLa9(SiO4)6O2, Crystallographic communications 75 (2019), https://doi.org/10.1107/S2056989019008442.
- [36] G. Costa, B.J. Harder, N.P. Bansal, J.L. Stokes, K. Lilova, T. Subramani, S. V. Ushakov, K.J. Meisner, A. Navrotsky, Energetics of reactions between ceramic coating materials and their binary oxide components with silicate melts, J. Am. Ceram. Soc. 105 (2022) 7795–7805, https://doi.org/10.1111/jace.18715.
- [37] G. Costa, B.J. Harder, N.P. Bansal, B.A. Kowalski, J.L. Stokes, Thermochemistry of calcium rare-earth silicate oxyapatites, J. Am. Ceram. Soc. 103 (2020) 1446–1453, https://doi.org/10.1111/jace.16816.
- [38] D.L. Poerschke, C.G. Levi, Effects of cation substitution and temperature on the interaction between thermal barrier oxides and molten CMAS, J. Eur. Ceram. Soc. 35 (2015) 681–691, https://doi.org/10.1016/j.jeurceramsoc.2014.09.006.
- [39] J.J.G. Chavez, R. Naraparaju, C. Mikulla, P. Mechnich, K. Kelm, C.V. Ramana, U. Schulz, Comparative study of EB-PVD gadolinium-zirconate and yttria-rich zirconia coatings performance against Fe-containing calcium-magnesiumaluminosilicate (CMAS) infiltration, Corros. Sci. 190 (2021) 109660, https://doi. org/10.1016/j.corsci.2021.109660.
- [40] K.T.M. Johnson, Experimental determination of partition coefficients for rare earth and high-field-strength elements between clinopyroxene, garnet, and basaltic melt at high pressures, Contrib. Mineral. Petrol. 133 (1998) 60–68.
- [41] E.H. Hauri, T.P. Wagner, T.L. Grove, Experimental and natural partitioning of Th, U, Pb and other trace elements between garnet, clinopyroxene and basaltic melts 117, Chem. Geol. (1994) 149–166, https://doi.org/10.1016/0009-2541(94)
- [42] B. Bonechi, C. Perinelli, M. Gaeta, A. Fabbrizio, M. Petrelli, L. Strnad, High pressure trace element partitioning between clinopyroxene and alkali basaltic melts, Geochem. Cosmochim. Acta 305 (2021) 282–305, https://doi.org/10.1016/j. gca.2021.04.023.
- [43] K. Shepherd, O. Namur, M.J. Toplis, J.-L. Devidal, B. Charlier, Trace element partitioning between clinopyroxene, magnetite, ilmenite and ferrobasaltic to dacitic magmas: an experimental study on the role of oxygen fugacity and melt composition, Contrib. Mineral. Petrol. 177 (2022) 90, https://doi.org/10.1007/ s00410-022-01957-y.

ARTICLE IN PRESS

C.Y. Guijosa-Garcia et al. Ceramics International xxx (xxxx) xxx

- [44] K.T.M. Johnson, Experimental cpx/and garnet/melt partitioning of REE and other trace elements at high pressures: petrogenetic implications, Mineral. Mag. 58A (1994) 454–455, https://doi.org/10.1180/minmag.1994.58A.1.236.
- [45] T.P. Paster, D.S. Schauwecker, L.A. Haskin, The behavior of some trace elements during solidification of the Skaergaard layered series, Geochem. Cosmochim. Acta 38 (1974) 1549–1577, https://doi.org/10.1016/0016-7037(74)90174-4.
- [46] J. Tuff, S.A. Gibson, Trace-element partitioning between garnet, clinopyroxene and Fe-rich picritic melts at 3 to 7 GPa, Contrib. Mineral. Petrol. 153 (2007) 369–387, https://doi.org/10.1007/s00410-006-0152-x.
- [47] M.G. Richter, Structure and possible origins of stacking faults in gamma-yttrium disilicate, Philos. Mag. 89 (2) (2009) 169–181, https://doi.org/10.1080/ 14786430802562132
- [48] A.C. Strzelecki, Y. Ren, S. Chong, B.J. Riley, H. Xu, J.S. McCloy, X. Guo, Structure and thermodynamics of calcium rare earth silicate oxyapatites, Ca2RE8(SiO4)6O2 (RE = Pr, Tb, Ho, Tm), Phys. Chem. Miner. 49 (2022) 13, https://doi.org/10.1007/s00269-022-01187-5
- [49] Y. Liu, Y. Liu, L. Zhuang, H. Yu, Y. Chu, Composition-driven superior CMAS corrosion resistance of high-entropy rare-earth disilicates, Corros. Sci. 233 (2024), https://doi.org/10.1016/j.corsci.2024.112108.
- [50] Y. Dong, K. Ren, Q. Wang, G. Shao, Y. Wang, Interaction of multicomponent disilicate (Yb0.2Y0.2Lu0.2Sc0.2Gd0.2)2Si2O7 with molten calcia-magnesiaaluminosilicate, J. Adv. Ceram. 11 (2022) 66–74, https://doi.org/10.1007/ s40145-021-0517-7.
- [51] C.Y. Guijosa-Garcia, in: Fakultät Maschinenwesen, Technische Universität Dresden,